Hindawi
Mathematical Problems in Engineering
Volume 2022, Article ID 6963982, 13 pages
https://doi.org/10.1155/2022/6963982

Research Article

Physical Model Test on the Influence of Karst Cave under and in front of Pile on the Stability of Embedded End of Antislide Pile

Jiahui Liang,[1] Qiuyan Fan ,[1] Menghan Liu,[2] and Tianyu Li[1]

[1]*Research Center of Geotechnical and Structural Engineering, Shandong University, Jinan, Shandong 250061, China*
[2]*School of Resources, Environment and Materials, Guangxi University, Nanning, Guangxi 530004, China*

Correspondence should be addressed to Qiuyan Fan; 202186000192@email.sdu.edu.cn

Received 27 February 2022; Accepted 15 April 2022; Published 28 May 2022

Academic Editor: Song Jiang

With the extensive use of antislide piles in engineering, the stability of the embedded end of antislide piles in karst areas has become increasingly prominent. When there is a cave in front of the antislide pile, the cave may be deformed under horizontal load, causing the stability of the embedded end of the antislide pile to lose its stability. Based on the similarity model theory, this study establishes two different shapes of caves (horizontal in the longitudinal direction and vertical in the longitudinal direction) beneath and in front of the rock-socketed section of the antislide pile. Using horizontal loading tests, the influence of the karst cave beneath and in front of the elliptical pile on the stability of the antisliding pile embedded end was studied, and the following relevant conclusions were obtained. (1) Compared with the model without cavities, the presence of cavities in front of and under the pile significantly reduces the horizontal bearing capacity of the antislip pile. The fracture trace initially develops from the bottom of the pile against the side of the active zone, roughly at 90° to the horizontal direction through the top plate of the cave and continues to develop under the cave until the boundary. (2) The horizontal bearing capacity of horizontal bearing pile is greatly reduced by karst cave. The karst cave under the pile has a greater influence on this property than that in front of pile and the influence of the two karst caves has a common effect. (3) Both sides of the bottom for pile and the roof of karst cave are prone to damage. Besides, the roof of the karst cave under the pile is more prone to damage for more obvious stress concentration. (4) The loading failure processes of all model can be roughly divided into three stages: gentle deformation, stable expansion of deformation, and accelerated expansion of deformation. (5) Compared with the case where there is no karst cave in front of pile, the karst cave in front of pile will increase the deformation of pile under horizontal load and the same level of load. (6) Based on the limit equilibrium method, a check calculation method for the bearing capacity of the anchored end when a cave existing in front of the pile is proposed. The verification method was verified.

1. Introduction

With the vigorous promotion of infrastructure and the increasing emphasis on the prevention and control of geological hazards in China, more and more foundation pit and landslide control projects have been carried out in typical karst development regions such as Guangxi, Guangdong, Guizhou, and Yunnan [1]. Supporting piles and antislide piles mainly subject to horizontal loads have been used massively in various projects, and the abovementioned two kinds of horizontal bearing piles are also widely applied in limestone with karst caves [2]. Therefore, the stability problem of horizontal bearing piles in karst regions is caused; however, in the face of such engineering problems, there are few engineering instances dealing with such a problem successfully. One of the main reasons is the severe shortage of study on theoretical foundation; as a result, when confronted with such a problem, people can merely seek for solutions through experience [3–5]. In conclusion, there is a relatively small number of research achievements on the horizontal bearing stability of pile foundation with karst caves around piles, and there are inadequate relevant technical specifications. Therefore, the study on the effect of karst caves beneath and in front of pile on the stability of embedded end of pile in this paper is of great significance [6–9]. Based on previous researches [10–12], this paper

carried out an indoor model test, analyzed the deformation and failure characteristics of karst cave models simultaneously existing beneath and in front of pile under the horizontal bearing, explored the effect mechanism of karst caves beneath and in front of pile on the embedded end of horizontal bearing pile, and constructed the corresponding stability calculation model.

2. Materials and Methods

2.1. Similar Model. When handling the three-dimensional space problem in practical projects, there have been relatively mature theories that simplify the row pile problem into the two-dimensional problem [13]. According to the first law of similarity theory, if the model is similar to the prototype system, and the geometric dimensions and physical quantities of the two are in a certain proportion mutually, the physical quantity of the model shall be determined, and then the corresponding quantity of the prototype can be deduced according to this proportion. The model test for this time was designed based on the condition that considered the body force, and the three constants restricted each other. If two of them were determined, the remaining one would be determined exclusively [14–16]. During the design, it was ascertained that the model dimension was produced as per the geometric similarity constant $C_l = 30$; then, based on the value of 1.3 for the physical similarity constant C_γ, according to $C_E = C_\sigma = C_\gamma C_l$, the stress similarity constant $C_\sigma = 39$ could be obtained. In addition, simulation materials conforming to the physical parameters and mechanical properties were selected as per this proportion to produce the model.

Finally, cement, gypsum, river sand, and barite powder were selected and used to produce the aggregate of the similar model. It was determined that the sand-binder ratio was 2.9 : 1, the water-paste ratio was 0.89 : 1, and the content of barite was 70.11%. Based on the existing construction experience of antislide piles in the karst regions, in the plain strain model, the test pile was set as the rigid pile, the hollow plate body welded by steel plate was used to simulate the pile body, and the pile occlusion was arranged continuously [17, 18].

The size and location of karst cave severely affect the stability of the embedded end of antislide pile. According to relevant data of antislide piles in karst regions [7], this paper simplified the karst cave into the elliptic and determined that the width of the long axis of karst cave was 3.5 m (model: 11.7 cm), the width of the short axis was 2 m (model: 6.7 cm), and the distance between karst cave and pile adopted the width of the short axis of karst cave, i.e., 2 m (model: 6.7 cm) (see Figure 1). See Table 1 for several important physical and mechanical properties and geometric parameters of prototype rock mass and model materials simulated by the test.

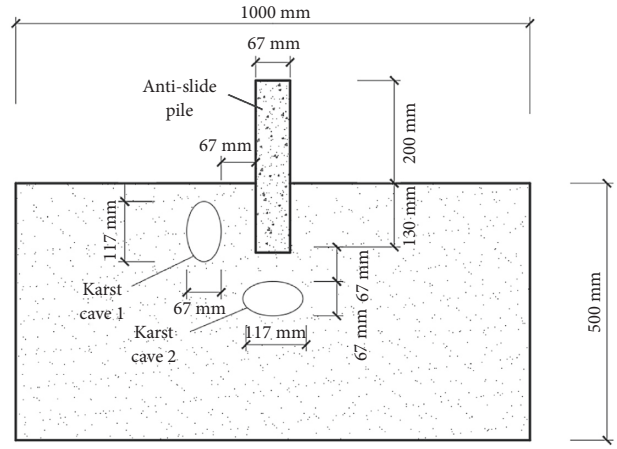

Figure 1: Schematic diagram of test model size.

3. Test Loading and Displacement Measurement

The loading location of horizontal load in this test was in the very center of pile on the surface of rock mass. The method of loading stage by stage was adopted, the load increment per stage was 0.2 kN, and relevant data recording should be conducted after each stage of load became stable. The loading was stopped when some model was destroyed, and the loading of the other model should be stopped after another stage of load was increased, so as to facilitate the comparative analysis. In the test, the Jack (DYG50-500) was used for loading, and the load capacity was displayed by the load sensor via the digital display instrument, as shown in Figure 2. The arrangement of material objects in the test was shown in Figure 3.

The displacement measuring points of embedded end and pile body in the model were as shown in Figure 4. The bedrock displacement change of rock-socketed section of antislide pile was measured by the dial indicator, so that the effect of karst cave on the embedded end stability of antislide pile could be further analyzed.

Arrangement in Figure 4: Dial Indicator 1 and Dial Indicator 3 were used to measure the deformation of rock mass surface in the active zone at the back of pile, which were arranged in the location 100 mm from the pile surface and 200 mm from the lateral edge of the model; Dial Indicator 4 and Dial Indicator 5 were used to measure the deformation of rock mass surface in the passive zone in front of pile, which were arranged in the location 200 mm from the pile surface and 200 mm from the lengthwise edge of the model; Dial Indicator 2 and Dial Indicator 6 were used to measure the horizontal displacement of the antislide pile, which was arranged in the location 100 mm from the top and 200 mm from the edge of the antislide pile; at the distance of 100 mm inward on the surface of both sides of the karst cave, one dial indicator should be arranged respectively along the horizontal axis of the karst cave to measure the convergence and deformation of cave diameter; the acoustic emission probes were arranged on both sides of the rock mass.

4. Results and Analysis

4.1. Analysis on the Deformation and Failure Characteristics. The loading results of karst cave model beneath and in front of pile were as shown in Figure 5. When it was loaded to 6.4 kN, the roof of the model karst cave would be destroyed,

Table 1: Physical and mechanical properties and geometric parameters of two materials.

	Geometric similarity constant						Physical similarity constant	Stress or strength similarity constant	
	Length of rock soil mass (m)	Width of rock soil mass (m)	Thickness of rock soil mass (m)	Length of antislide pile (m)	Pile width (m)	Rock-socketed depth (m)	Unit weight of limestone (kN/m^3)	Compressive strength of limestone (MPa)	Tensile strength (MPa)
Prototype rock mass	30	15	18	10	2	4	27	70	8
Similar material	1	0.5	0.6	0.33	0.067	0.13	20.77	1.79	0.21

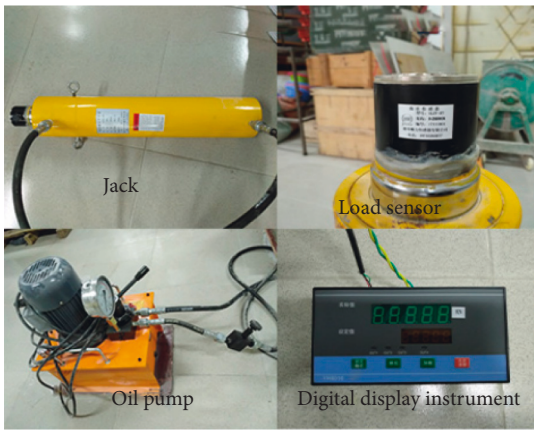

Figure 2: Loading system.

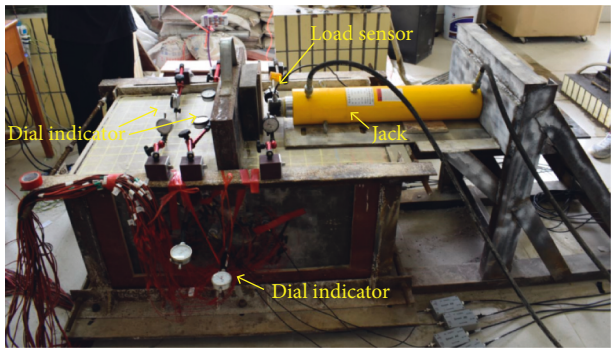

Figure 3: Physical map of horizontal and long axis karst cave model device.

and the crack generated would start extending from the pile bottom near the passive zone and expand towards the direction of the karst cave, finally forming the fracture surface. The fracture surface is about 90° from the horizontal direction, and it could be judged that the embedded end of pile lost the bearing capacity.

The data of each dial indicator were collected, and each load-displacement curve of the model as shown in Figure 6 was obtained after statistics.

(1) According to Figure (a): The pile displacement was the smallest when the model was in the loading stage of 0 kN-1.0 kN. The reason for the appearance of this phenomenon was that the material densities of the upper and lower parts of the model were different due to the effect of body force in the mixing and grouting process of the simulation material; therefore, the filling of aggregate was insufficient and caused a part of pores in the upper-layer model. Thus, this stage was the model compaction stage; when the model was within the loading range of 1.0 kN-3.2 kN, the increment of horizontal displacement value in this stage would increase at a constant speed with the increasing of load. It was analyzed and considered that the inner pores and microcracks inside the model were developing steadily at the moment; 3.2 KN-6.4 KN (failure load): The speed increase of horizontal displacement of pile body in this stage increased obviously, from the perspective of load-displacement curve, it was manifested that the slope of curve increased continuously, and the cracking sound from inside the model became more intense. Although no observable cracks appeared on the model surface in the loading process, when the load was increased to the failure load gradually, the model had cracks and failure in an instant. It was analyzed and considered that the cracks of the model in this stage were accelerating and expanding. It could be found from Figure 6(d) that the convergence and displacement of the roof of karst cave beneath the model pile also had three similar stages. Therefore, the deformation failure process of the model under the horizontal load could be roughly divided into three stages, which were model compaction, stable expansion of cracks, and accelerated expansion of cracks.

(2) According to Figure 6(b) and Figure 6(c): With the load being applied to the pile body, both of the rock mass surfaces in front of and at the back of the model pile body had the phenomenon of bump. Then the displacements were compared. When the load was smaller, under the load of the same grade, the rock mass displacement of the passive zone in front of pile was smaller than that of the active zone at the back of pile. When the load was bigger, the rock mass displacement in the passive zone at the back of pile increased rapidly and had little difference with the rock mass displacement of the active zone at the back of pile. It could be seen that the reaction speed of the rock mass displacement in the passive zone in front

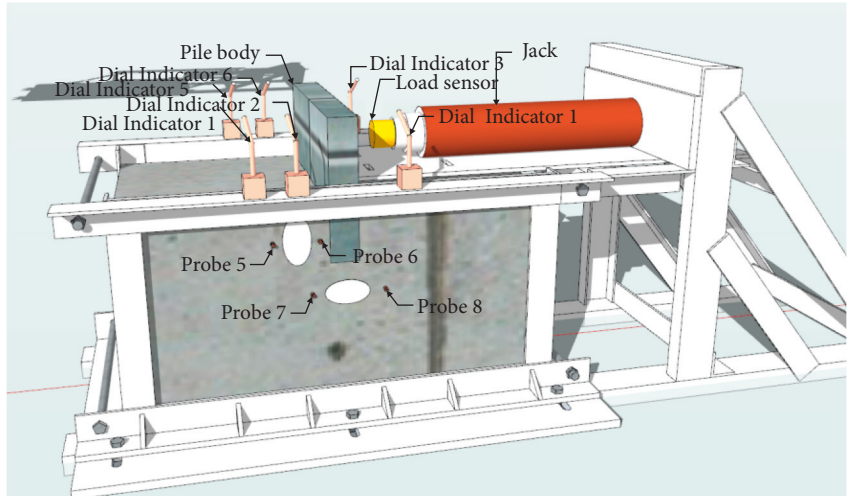

Figure 4: Schematic diagram of measuring point location of longitudinal axis karst cave model.

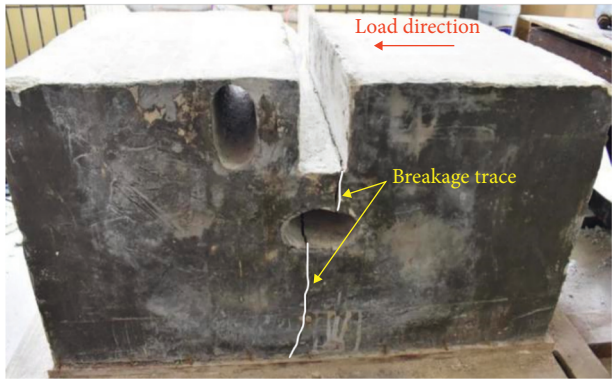

Figure 5: Destruction of the model.

of pile to the horizontal load was smaller than that at the back of pile. In the loading process, both of the rock masses in front of and at the back of pile had deformations, but the displacements were smaller, and the difference was not much. The displacement remained stable after the loading entered the later stage, which explained that the rock masses in front of and at the back of pile were not destroyed when they were loaded to the failure load of the model.

(3) According to Figure 6(d): Both of the horizontal axis of karst cave in front of pile and that beneath the pile had convergence and deformation, but the deformation characteristics of the two karst caves had difference. In the whole loading process, the relative distance of the horizontal axis of karst cave beneath the pile could be divided into three stages according to the deformation rate, which were slow deformation, stable deformation, and intensified deformation. The loading intervals of the three stages were 0 KN-1.0 KN, 1.0 KN-3.2 KN, and 3.2 KN-6.4 KN (failure load), respectively. The convergence of karst cave in front of pile started to keep the linear growth after reaching 1.0 KN, and the growth rate did not change much in the process of reaching the failure load. It could be seen that the karst cave in front of pile still had not reached the stage of accelerated deformation when the karst cave beneath the pile reached the failure load, and the karst cave beneath the pile reached the third stage in advance, i.e., crack acceleration and expansion stage.

4.2. Comparison and Verification of Simulation and Test Results for Bearing Capacity of Test Pile with Karst Cave under and in front of It. A simulation study on the bearing capacity of antislide piles with karst caves under and in front of pile has been carried out by our research group. In this work, the analysis results in the simulation test are used to verify the results of similar indoor model tests in this article and analyze the influence of karst caves under and in front of pile on the bearing capacity of antislide pile. With reference to the results of other researchers in our group which determine five factors of the thickness of roof of the karst cave in front of pile, the distance between the karst cave in front of the pile and the side of pile, the distance between karst cave under the pile and the end of the pile, and the span-height ratio of the karst cave in front of and under the pile as variable parameters through staged loading simulation of antislide, the orthogonal design is used in this research to group the parameters and perform simulation tests, respectively, to obtain the horizontal ultimate load of the antislide pile under each group of tests and analyze the influence of variable factors on the bearing capacity of antislide piles. The horizontal load-bearing capacity and divisions of various factor of this study are shown in Table 2.

According to the factors listed above, SPSS software is used to carry out mixed level orthogonal experiment design and obtain a total of 49 sets of parameter combinations, as shown in Table 3

Through calculation of 49 sets parameter combinations above, the displacement of the contact point between the pile and the front rock mass is recorded and a displacement curve is produced based on that. In addition, the starting

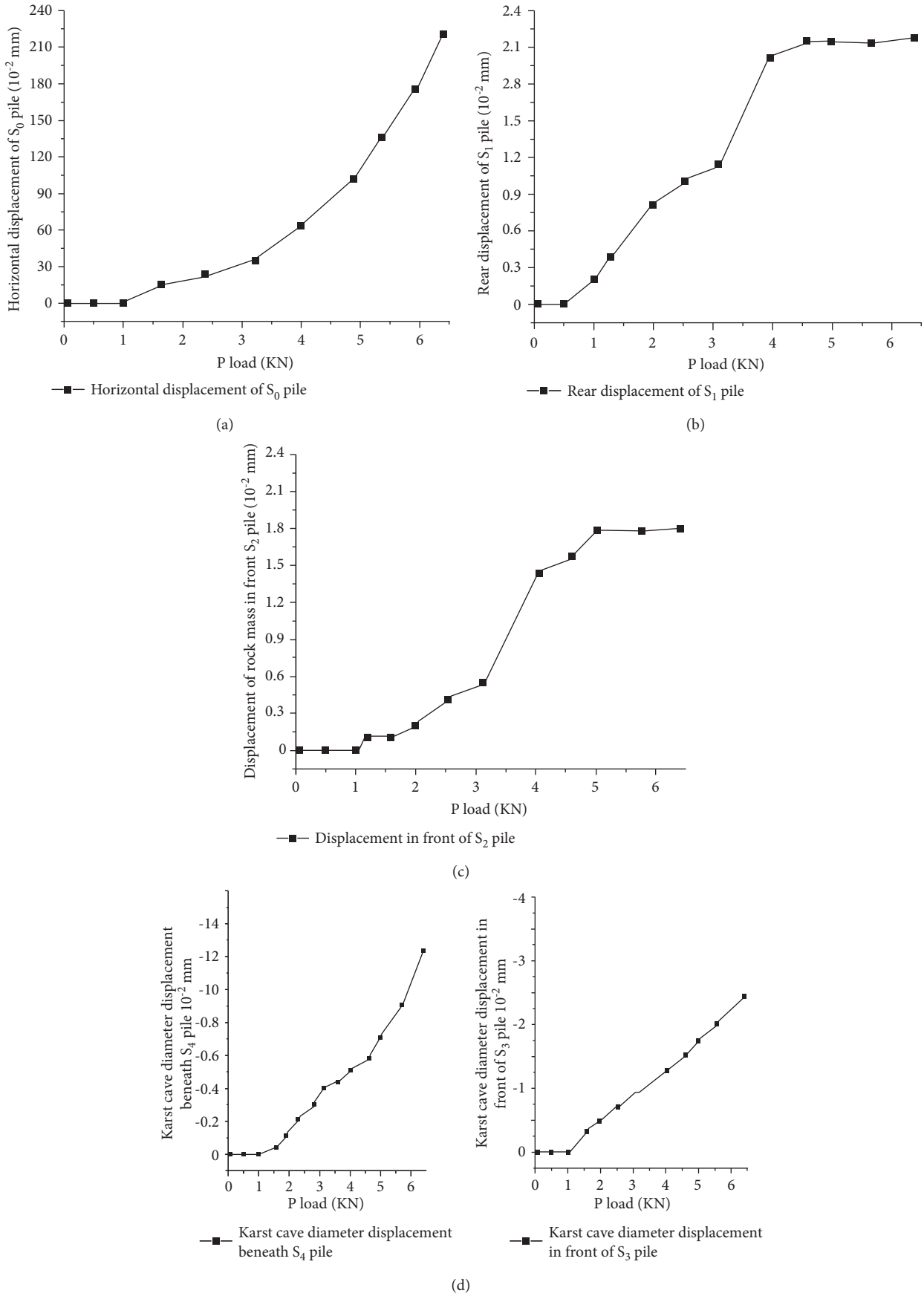

Figure 6: Load-displacement curve. (a) Horizontal displacement of pile. (b) Comparison of bump displacement at the back of pile. (c) Comparison of bump displacement in front of pile. (d) Comparison of karst cave convergence.

Table 2: Orthogonal test design of each factor for horizontal load-bearing pile.

Group number	A	B	C	D	E
1	1.60	1.60	0.30	0.6	1.22
2	1.60	0.80	1.60	0.82	1.67
3	0.80	1.20	2.00	0.82	2.5
4	1.20	2.00	1.20	2.5	2.5
5	1.20	1.60	2.00	1.22	0.82
6	2.40	0.40	1.20	0.82	1.22
7	0.40	1.20	1.20	1.67	1.67
8	1.20	0.80	0.90	1.67	1.22
9	2.00	2.00	0.30	0.82	0.4
10	1.20	1.20	0.30	0.4	2.5
11	0.40	0.40	0.30	1.67	0.6
12	2.40	0.40	2.00	2.5	0.4
13	0.40	0.80	2.00	0.6	0.6
14	0.40	2.40	1.60	2.5	2.5
15	1.60	2.00	2.00	1.67	2.5
16	2.00	0.40	1.20	0.6	2.5
17	0.80	1.60	1.20	2.5	0.6
18	2.40	2.00	0.90	0.4	0.6
19	1.20	2.40	0.60	0.82	0.6
20	0.80	0.40	0.90	1.22	2.5
21	0.80	0.40	1.60	0.4	1.22
22	1.60	2.40	1.20	0.4	0.82
23	0.40	2.00	1.60	2.5	0.82
24	2.40	0.80	0.60	2.5	2.5
25	2.40	1.20	0.30	0.6	0.82
26	0.40	0.40	0.30	2.5	2.5
27	0.40	1.20	0.60	2.5	1.22
28	0.80	2.00	0.60	0.6	1.67
29	2.40	2.40	0.30	1.22	1.67
30	2.00	2.40	2.00	2.5	1.22
31	1.20	0.40	0.30	2.5	1.67
32	0.80	0.80	0.30	2.5	0.82
33	0.40	2.40	0.90	0.6	2.5
34	2.00	0.80	0.30	0.4	2.5
35	1.60	0.40	0.30	2.5	0.6
36	1.60	1.20	0.90	2.5	0.4
37	1.60	0.40	0.60	1.22	2.5
38	0.40	2.00	0.30	1.22	1.22
39	0.40	1.60	0.30	0.82	2.5
40	2.00	1.20	1.60	1.22	0.6
41	2.40	1.60	1.60	1.67	2.5
42	0.40	0.40	0.90	0.82	0.82
43	2.00	1.60	0.90	2.5	1.67
44	2.00	0.40	0.60	1.67	0.82
45	1.20	0.40	1.60	0.6	0.4
46	0.40	1.60	0.60	0.4	0.4
47	0.40	0.80	1.20	1.22	0.4
48	0.40	0.40	2.00	0.4	1.67
49	0.80	2.40	0.30	1.67	0.4

point of the obvious steep drop in the displacement curve is set as horizontal ultimate load. The horizontal ultimate load and the horizontal displacement value of the contact point for the pile and the front rock mass as the ultimate load is reached are determined under each group of parameters combination and shown in Table 4.

Finally, the multiple linear regression equation of each factor influence on the horizontal ultimate load is obtained through linear regression method as shown in

$$Y = 1.014X_1 + 0.283X_2 - 0.058X_3 - 0.053X_4 - 0.017X_5 + 1.426. \quad (1)$$

The applicable conditions of (1) are as follows: the strength and stability of antislide pile meet the safety requirements, the structure of the bedrock is complete except for the karst caves, the rock mass is uniform, there is no development of large joints and cracks, and there are no other high-strength fillers inside the karst caves. The formula can be used to preliminarily estimate the horizontal bearing capacity of antislide pile as the karst cave existing when all the conditions above are met. In the formula, X1~X5 should conform to the value range of each factor in the orthogonal experimental design. Besides, to ensure the unity of dimensions, the coefficient unit of X1~X3 is defined as MN/m^3 and X4~X5 are dimensionless factors where the unit of their coefficients and constant term is defined as MN/m^2. The various parameters of prototype rock mass in the indoor model test in this article are substituted into formula (1), obtaining the simulated ultimate load value and comparing it with the test results. In addition, the simulated load value obtained by formula (1) is then converted into the form of concentrated force for test model and the verification results are shown in Table 5.

It can be seen that the error between the calculated and test load is relatively small which proves that the simulation conclusion is consistent with that obtained from this experiment. Accordingly, this formula can also successfully reflect the influence of karst caves under and in front of pile on the bearing capacity of antislide piles in actual project.

4.3. Comparative Analysis of the Test Results for the Model with Karst Caves under and in front of Piles with the Other Three Types of Models. In order to analyze the influence of karst cave under and in front of the pile at the same time on the horizontal bearing capacity of antislide pile, as well as the bearing mechanism and failure mode of pile foundation in this case, the non-karst cave model, karst cave in front of the pile model, karst cave under the pile, and karst cave in front of and under the pile model are all used to do comparative analysis. The related instruments and meters of other models are arranged similarly to the most unfavorable situation. Specifically, two dial gauges are used to measure the uplift displacement of active zone for rock mass behind pile. Besides, two dial gauges are used to measure the horizontal displacement of antislide pile and the other two dial gauges are used to measure the uplift displacement of passive zone for rock mass in front of the pile. In addition, the model with karst caves also measures the convergence of them. Acoustic emission phenomenon monitoring points are also located on both sides of karst cave where damage is easy to occur.

5. Experiment Setup

The test objects of non-karst cave model, the karst cave in front of the pile model, and the karst cave under the pile model are shown in Figure 7. The layout of the

Table 3: Orthogonal test design of horizontal bearing pile.

Group number	A	B	C	D	E
1	1.60	1.60	0.30	0.6	1.22
2	1.60	0.80	1.60	0.82	1.67
3	0.80	1.20	2.00	0.82	2.5
4	1.20	2.00	1.20	2.5	2.5
5	1.20	1.60	2.00	1.22	0.82
6	2.40	0.40	1.20	0.82	1.22
7	0.40	1.20	1.20	1.67	1.67
8	1.20	0.80	0.90	1.67	1.22
9	2.00	2.00	0.30	0.82	0.4
10	1.20	1.20	0.30	0.4	2.5
11	0.40	0.40	0.30	1.67	0.6
12	2.40	0.40	2.00	2.5	0.4
13	0.40	0.80	2.00	0.6	0.6
14	0.40	2.40	1.60	2.5	2.5
15	1.60	2.00	2.00	1.67	2.5
16	2.00	0.40	1.20	0.6	2.5
17	0.80	1.60	1.20	2.5	0.6
18	2.40	2.00	0.90	0.4	0.6
19	1.20	2.40	0.60	0.82	0.6
20	0.80	0.40	0.90	1.22	2.5
21	0.80	0.40	1.60	0.4	1.22
22	1.60	2.40	1.20	0.4	0.82
23	0.40	2.00	1.60	2.5	0.82
24	2.40	0.80	0.60	2.5	2.5
25	2.40	1.20	0.30	0.6	0.82
26	0.40	0.40	0.30	2.5	2.5
27	0.40	1.20	0.60	2.5	1.22
28	0.80	2.00	0.60	0.6	1.67
29	2.40	2.40	0.30	1.22	1.67
30	2.00	2.40	2.00	2.5	1.22
31	1.20	0.40	0.30	2.5	1.67
32	0.80	0.80	0.30	2.5	0.82
33	0.40	2.40	0.90	0.6	2.5
34	2.00	0.80	0.30	0.4	2.5
35	1.60	0.40	0.30	2.5	0.6
36	1.60	1.20	0.90	2.5	0.4
37	1.60	0.40	0.60	1.22	2.5
38	0.40	2.00	0.30	1.22	1.22
39	0.40	1.60	0.30	0.82	2.5
40	2.00	1.20	1.60	1.22	0.6
41	2.40	1.60	1.60	1.67	2.5
42	0.40	0.40	0.90	0.82	0.82
43	2.00	1.60	0.90	2.5	1.67
44	2.00	0.40	0.60	1.67	0.82
45	1.20	0.40	1.60	0.6	0.4
46	0.40	1.60	0.60	0.4	0.4
47	0.40	0.80	1.20	1.22	0.4
48	0.40	0.40	2.00	0.4	1.67
49	0.80	2.40	0.30	1.67	0.4

measurement equipment for each model is similar to the karst cave under and in front of pile model which has been described above.

6. Comparison of Test Damage Results

Similar to the karst cave under and in front of the pile model, the other three types of models are also equipped with high-frequency cameras to record all loading processes. Specifically, the conditions of the non-karst cave model, the karst cave in front of the pile model, and the karst cave under the pile model after being loaded to failure are shown in Figure 8 according to the recording of high-frequency camera.

Observing the change characteristics of other three types of models during the entire loading process recorded by high-frequency camera, it can be seen that there is no visible crack growth on the surface of each model before reaching failure load. However, all models have recorded a crisp sound of rupture during the loading process which may be caused by the internal cracks of the model. Besides, the sound is more obvious in the later stage of test as the continuous increase of load. As each model is loaded to the failure value, it shows brittle fracture instantly and is accompanied by sound. The pile body loses stability afterwards. Table 6 shows the main conditions during the loading process of non-karst cave model, karst cave in front of the pile model, and karst cave under the pile model.

Under similar test conditions, conclusions can be drawn from information in the table.

(1) The ultimate load of non-karst cave model is up to 11.25 KN and the ultimate load of karst cave in front of pile model is reduced to about 68% of 11.25 KN. However, the ultimate load of karst cave under the pile model can only reach about 58.0% and the ultimate load of karst cave under and in front of the pile model is the smallest, accounting for only 56.9% of the non-karst cave cases which is 1.1% decrease on the basis of the karst cave under the pile model. In summary, it can be seen that the karst cave under and in front of the pile model has the greatest influence on horizontal bearing capacity of antislide pile and the influence of karst cave under the pile on the horizontal bearing capacity for the antislide pile is greater than that of karst cave in front of the pile. Besides, the influence of two karst caves has a combined effect.

(2) The initial development positions of cracks are mainly concentrated in two areas, namely, the bottom of the pile which is close to active area behind the pile and the roof of karst cave. Comparing the karst cave under the pile model and the non-karst cave model, the bottom of pile which is near the back of pile is more prone to damage. However, when there is karst development under the pile, the roof of karst cave increases the stress concentration phenomenon. Therefore, it can be seen that the ultimate bearing capacity of model piles with karst caves under the piles is lower than that of other models in the test.

(3) From the perspective of crack development, the rock mass at the embedded end of antislide pile is mostly tensile failure under horizontal load. Only when there is a karst cave in front of the pile, it shows compression failure. It is speculated that the difference between tensile and compressive strength is large and the roof of karst cave under the pile is tensioned, resulting in that the influence of karst cave under the pile on horizontal bearing capacity of antislide pile is greater than that of the cave in front of pile.

Table 4: Orthogonal test results of horizontal load-bearing piles.

Group number	Horizontal ultimate load	The horizontal displacement value of the contact point for the pile and the front rock mass
1	3.8	−1.09E-02
2	3.4	−9.55E-03
3	2.4	−6.00E-03
4	3.0	−7.48E-03
5	3.4	−1.02E-02
6	3.6	−9.53E-03
7	1.4	−3.91E-03
8	2.6	−6.09E-03
9	3.6	−9.77E-03
10	3.4	−1.01E-02
11	1.6	−8.39E-03
12	3.8	−1.10E-02
13	1.6	−4.75E-03
14	2.2	−6.38E-03
15	3.6	−9.65E-03
16	3.6	−9.75E-03
17	2.2	−5.20E-03
18	3.6	−9.43E-03
19	3.6	−1.01E-02
20	1.6	−3.35E-03
21	2.2	−5.84E-03
22	3.6	−9.64E-03
23	2.0	−6.48E-03
24	3.6	−9.94E-03
25	3.8	−1.09E-02
26	1.2	−3.58E-03
27	1.4	−4.08E-03
28	3.4	−9.93E-03
29	3.6	−9.48E-03
30	4.2	−1.27E-02
31	3.4	−9.27E-03
32	2.6	−9.04E-03
33	3.0	-8.69E-03
34	3.6	−9.94E-03
35	3.6	−9.86E-03
36	3.6	−1.08E-02
37	3.6	−9.79E-03
38	2.2	−6.34E-03
39	1.8	−4.98E-03
40	3.6	−9.44E-03
41	3.8	−1.03E-02
42	1.8	−1.26E-02
43	3.6	−9.31E-03
44	3.6	−9.68E-03
45	2.8	−7.27E-03
46	2.4	−6.57E-03
47	1.6	−6.26E-03
48	1.6	−5.26E-03
49	3.2	−8.28E-03

Note. The load unit in the table is MPa, and the displacement unit is *m*.

Table 5: Verification results of horizontal ultimate bearing capacity.

Type	Simulated ultimate load value by formula (1)	Test ultimate load value (KN)
Karst cave under and in front of pile test model	6.9	6.2

Note. The previous load of the failure load is taken as ultimate load of the test.

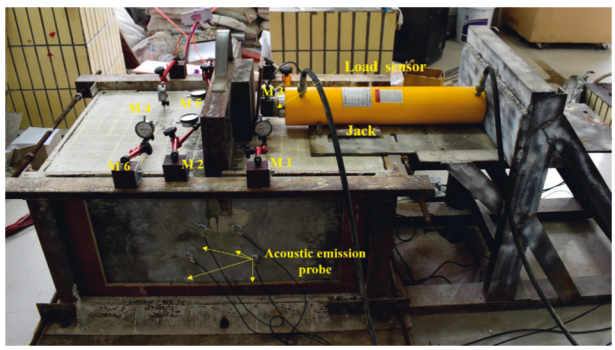

(a)

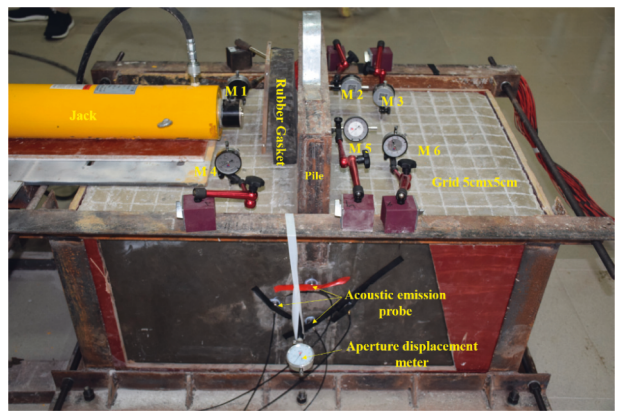

(b)

(c)

FIGURE 7: Layout of other three types of models: (a) non-karst cave model; (b) karst cave under the pile model; (c) karst cave in front of the pile model.

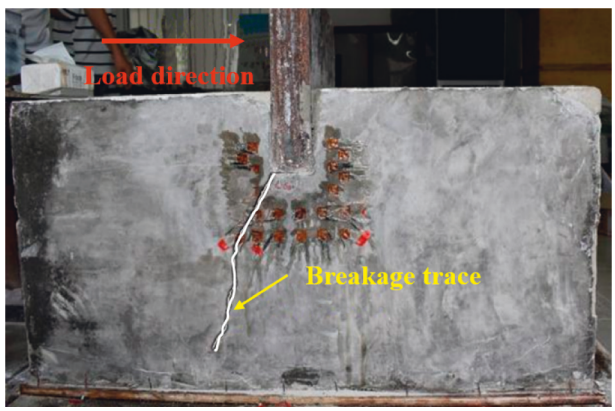

(a)

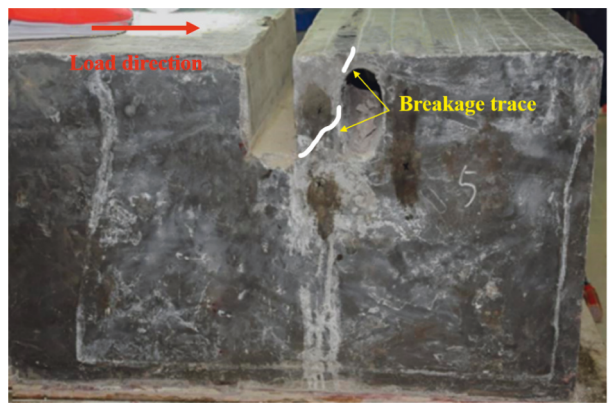

(b)

FIGURE 8: Continued.

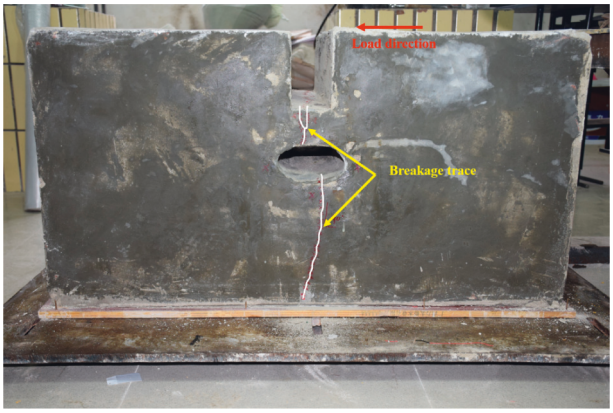

(c)

Figure 8: Failure conditions of the other three types of models: (a) non-karst cave model; (b) karst cave under the pile model; (c) karst cave in front of the pile model.

Table 6: Comparative analysis of damage conditions for each model.

Operating conditions	Failure load (KN)	Initial crack development position	Crack growth pattern	Model failure mode
Karst cave under and in front of pile model	6.4	The bottom of the pile which is close to the active area behind pile	Penetrating the roof of the karst cave at approximately 90° from the horizontal	Damaged by tension
Karst cave under pile model	6.52	The bottom of the pile which is close to the active area behind pile	Penetrating the roof of the karst cave at approximately 90° from the horizontal	Damaged by tension
Karst cave in front of pile model	7.60	The surface of rock mass on the roof of karst cave in front of the pile	Penetrating the roof of the karst cave at approximately 45° from the horizontal	Damaged by pressure
Non-karst cave model	11.25	The bottom of the pile which is close to the active area behind pile	Extend to the back of pile at 60° from the horizontal	Damaged by tension

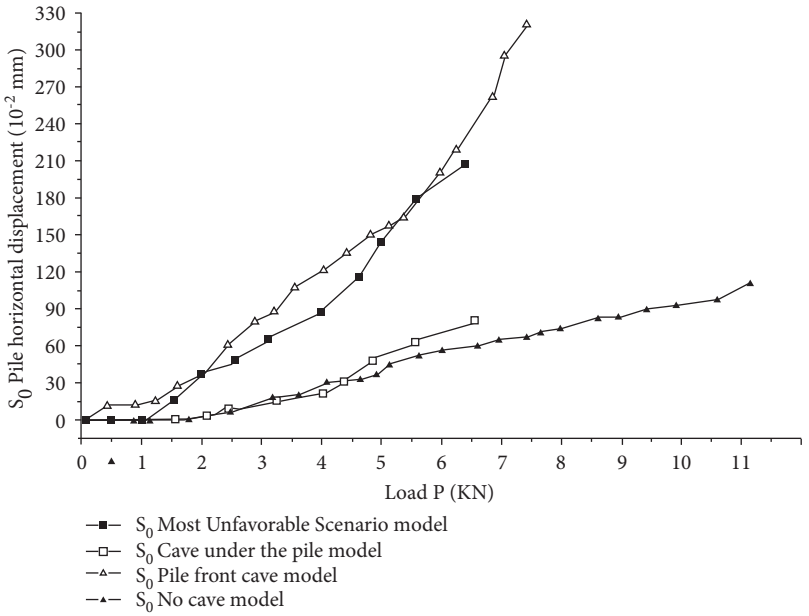

Figure 9: P-S_0 curve comparison chart of each model.

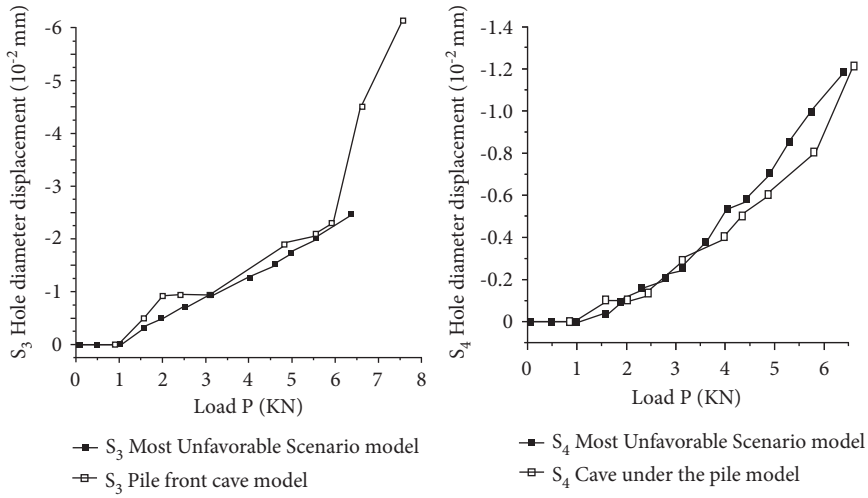

FIGURE 10: P–S_3(S_4) curve comparison chart of the horizontal axis of karst cave.

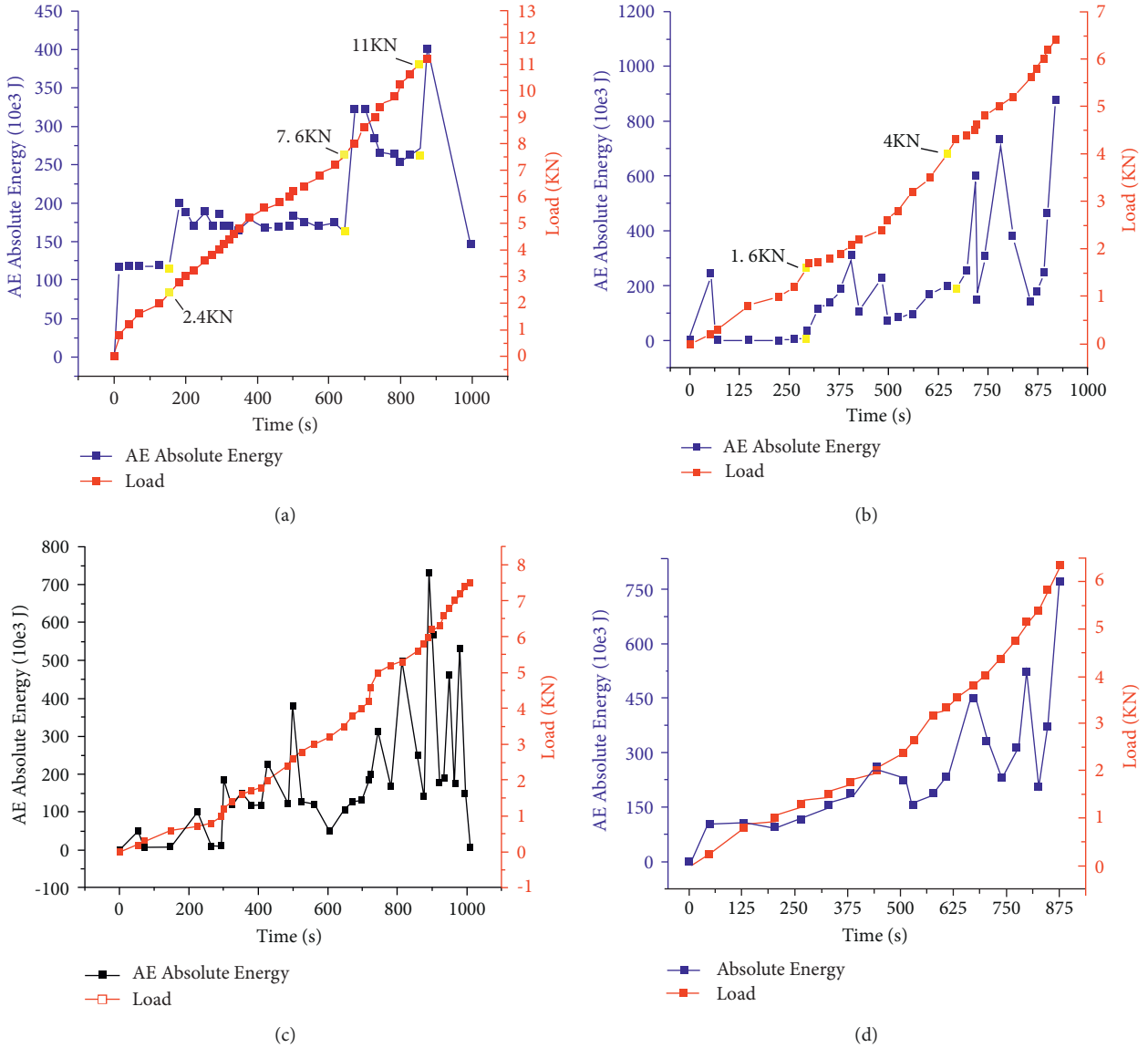

FIGURE 11: Comparison of acoustic emission phenomena of various models. (a) Non-karst cave model; (b) karst cave under the pile model; (c) karst cave in front of the pile model; (d) karst cave under and in front of the pile model.

7. Quantitative Analysis and Comparison of the Destruction Process of Each Model

7.1. P-S_0 Curve. The comparison diagram of load-displacement curve of horizontal displacement for each model pile is drawn according to the data recorded in the corresponding measured pile displacement percentage table for each model, as shown in Figure 9. S_0 refers to pile horizontal displacement. It can be analyzed from the figure below:

①The displacement of the pile during loading process for each model can be roughly divided into three stages: slow displacement growth is the initial stage, linear displacement growth is the middle stage, and the accelerated displacement growth is the last stage.

②The displacement of model pile with a karst cave in front of pile is relatively large under the same load. Herein, it can be seen that the karst cave in front of pile has great influence on the horizontal displacement of antislide pile that its existence will increase this value.

7.2. P-S_3(S_4) Curve. The convergence of karst cave diameter during the loading process is also measured for every model with karst caves and the comparison diagram of load-displacement curves for the karst cave in front of pile and under the pile in different models is finished, as shown in Figure 10. S_3 and S_4 refer to the hole diameter displacements of caves in front of and under the pile. The positive value indicates an increase in the diameter of karst cave and negative value indicates a decrease trend on the contrary. It can be analyzed from the figure below:

①The diameter of karst cave on horizontal axis maintains a convergence trend under horizontal loads.

②The convergence curve for diameter of karst cave that has reached failure can also be roughly divided into three stages: slow change of the hole diameter, stable change of the hole diameter, and accelerated change of the hole diameter.

7.3. Comparative Analysis of Acoustic Emission. The absolute energy curve of acoustic emission corresponding to loading process for model with karst cave under and in front of the pile and the other three types are shown in Figure 11.

It can be seen that the absolute energy performance of acoustic emission for all models has similar periodic laws.

(i) ①The preloading stage is the compacting stage of microcracks inside the model rock mass. The initial energy intensity is relatively stable with small fluctuations with continuous increase of horizontal load.

(ii) ②In the stage of stable crack propagation, the damage inside the rock mass continues to intensify and the crack develops steadily as the horizontal load increases during this stage. The acoustic emission event increases slowly and steadily. Besides, the energy intensity stabilizes at a medium-to-high level.

(iii) ③During the accelerated failure stage of cracks, as the internal cracks intensify, local strain energy is rapidly released during the stress process of rock mass, forming a strong acoustic emission signal, showing a step increase in the energy curve and the energy intensity fluctuating more than the peak intensity. The subsequent fall is at a relatively stable high level and the specimen model is directly damaged. This failure time can correspond to the failure time of load energy relationship and the displacement load curve of pile described above.

8. Conclusion

(1) Compared with the model without cavities, the presence of cavities in front of and under the pile significantly reduces the horizontal bearing capacity of the antislip pile. The fracture trace initially develops from the bottom of the pile against the side of the active zone, roughly at 90° to the horizontal direction through the top plate of the cave, and continues to develop under the cave until the boundary.

(2) The horizontal bearing capacity of horizontal bearing pile is greatly reduced by karst cave. The karst cave under the pile has a greater influence on this property than that in front of pile and the influence of the two karst caves has a common effect. Both sides of the bottom for pile and the roof of karst cave are prone to damage. Besides, the roof of the karst cave under the pile is more prone to damage for more obvious stress concentration.

(3) The loading failure processes of all model can be roughly divided into three stages: gentle deformation, stable expansion of deformation, and accelerated expansion of deformation. Compared with the case where there is no karst cave in front of pile, the karst cave in front of pile will increase the deformation of pile under horizontal load and the same level of load.

(4) Based on the limit equilibrium method, a check calculation method for the bearing capacity of the anchored end when a cave exists in front of the pile is proposed. The error between the fitting results and the experimental results is small.

Data Availability

The figures and tables used to support the findings of this study are included within the article.

Conflicts of Interest

The authors declare that they have no conflicts of interest.

Acknowledgments

The authors would like to show sincere thanks to those technicians who have contributed to this research.

References

[1] Y. S. Shen, P. Wang, M. P. Li, and Q. W. Mei, "Application of subway foundation pit engineering risk assessment: a case study of Qingdao rock area, China," *KSCE Journal of Civil Engineering*, vol. 23, no. 11, pp. 4621–4630, 2019.

[2] J. Lai, Y. R. Zheng, Y. Liu, X. D. Li, and H. W. Liu, "Seismic design of multiple anti-slide piles by strength reduction dynamics analysis method," *Electronic Journal of Geotechnical Engineering*, vol. 20, no. 5, pp. 1725–1737, 2015.

[3] R. P. West, M. E. Heelis, M. N. Pavlović, and G. B. Wylie, "Stability of end-bearing piles in a non-homogeneous elastic foundation," *International Journal for Numerical and Analytical Methods in Geomechanics*, vol. 21, pp. 845–861, 1997.

[4] T. Yamagami, J. C. Jiang, and K. Ueno, "A limit equilibrium stability analysis of slopes with stabilizing piles," in *Proceedings of the Slope Stability 2000*, pp. 343–354, Denver, Colorado, August 2000.

[5] Z. Datong, "Stability of friction-bearing piles," *Chinese Journal of Rock Mechanics and Engineering*, vol. 23, no. 12, pp. 2106–2109, 2004.

[6] C. Y. Lee, T. S. Hull, and H. G. Poulos, "Simplified pile-slope stability analysis," *Computers and Geotechnics*, vol. 17, no. 1, pp. 1–16, 1995.

[7] C. K. Choy, J. R. Standing, and R. J. Mair, "Stability of a loaded pile adjacent to a slurry-supported trench," *Géotechnique*, vol. 57, no. 10, pp. 807–819, 2007.

[8] A. F. Ramirez-Henao and J. Paul Smith-Pardo, "Elastic stability of pile-supported wharves and piers," *Engineering Structures*, vol. 97, pp. 140–151, 2015.

[9] F. Cai and K. Ugai, "Numerical analysis of the stability of a slope reinforced with piles," *Soils and Foundations*, vol. 40, no. 1, pp. 73–84, 2000.

[10] S. J. Gao, L. C. Wang, and W. Long, "Variation of the ultimate bearing capacity of karst cave roof under the loading of pile foundation," *Electronic Journal of Geotechnical Engineering*, vol. 19, pp. 8467–8483, 2014.

[11] S. Jiang, M. Huang, T. Fang, W. Chen, and X. Shangguan, "A new large step-tapered hollow pile and its bearing capacity," *Proceedings of the Institution of Civil Engineers-Geotechnical Engineering*, vol. 173, no. 3, pp. 191–206, 2020.

[12] X. Wei, Y. Guo, H. Cheng, J. Wei, L. Huo, and Z. Hou, "Estimation of fracture geometry parameters and characterization of rock mass structure for the Beishan Area, China," *Acta Geologica Sinica-English Edition*, vol. 94, no. 5, pp. 1381–1392, 2020.

[13] C. Jiang, M. H. Zhao, and W. G. Cao, "Stability analysis of subgrade cave roofs in karst region," *Journal of Central South University of Technology*, vol. 15, no. S2, pp. 38–44, 2008.

[14] C. Jiang, L. Liu, and J. P. Wu, "A new method determining safe thickness of karst cave roof under pile tip," *Journal of Central South University*, vol. 21, no. 3, pp. 1190–1196, 2014.

[15] Z. K. Hou, H. L. Cheng, S. W. Sun, J. Chen, D. Q. Qi, and Z. B. Liu, "Crack propagation and hydraulic fracturing in different lithologies," *Applied Geophysics*, vol. 16, no. 2, pp. 243–251, 2019.

[16] G. Y. Gao, Z. Y. Li, C. Qiu, and Z. Q. Yue, "Three-dimensional analysis of rows of piles as passive barriers for ground vibration isolation," *Soil Dynamics and Earthquake Engineering*, vol. 26, no. 11, pp. 1015–1027, 2006.

[17] R. Zhang, "Dealing with karst foundation by manual holing pouring piles techniques," *Shanxi Architecture*, vol. 36, no. 16, pp. 68-69, 2010.

[18] M. Y. Fattah and W. H. Al-Soudani, "Bearing capacity of open-ended pipe piles with restricted soil plug," *Ships and Offshore Structures*, vol. 11, no. 5, pp. 501–516, 2016.